Cell-Centered Nonlinear Finite-Volume Methods With Improved Robustness

Wenjuan Zhang and **Mohammed Al Kobaisi,** Khalifa University of Science and Technology

Summary

We present a nonlinear finite-volume method (NFVM) that is either positivity-preserving or extremum-preserving with improved robustness. The key ingredient of the method is the construction of one-sided fluxes, which involves decomposition of conormal vectors by introducing harmonic-averaging points as auxiliary points. The original NFVM using harmonic-averaging points is not robust in the sense that decomposition of conormal vectors with nonnegative coefficients can easily run into difficulties for heterogeneous and anisotropic permeability tensors on general nonorthogonal meshes. To improve NFVM robustness, we first present an alternative derivation of harmonic-averaging points and give a different formula that shows more clearly a point's location. On the basis of the derivation of the new formula, a correction algorithm is proposed to make modifications to those problematic harmonic-averaging points so that all the conormal vectors can be decomposed with nonnegative coefficients successfully. As a result, the resulting NFVM can be applied to more-challenging problems when conormal decomposition with nonnegative coefficients is not possible without correction. The correction algorithm is a compromise between robustness and accuracy. While it improves the robustness of the resulting NFVM, results of numerical convergence tests show that the effect of our correction algorithm on accuracy is problem-dependent. Optimal order of convergence is still maintained for some problems, and the convergence rate is reduced for others. Monotonicity and extremum-preserving properties are verified by numerical experiments. Finally, a field test case is used to demonstrate that the NFVM combined with our correction algorithm can be applied to simulate real-life reservoirs of industry-standard complexity.

Introduction

Accurate and robust modeling of heterogeneous and highly anisotropic diffusion processes on possibly severely distorted meshes poses serious challenges to numerical discretization methods and has been an area of active research for decades. In petroleum-reservoir simulation, for example, reliable prediction of reservoir dynamics requires a simulator that can rigorously handle highly heterogeneous and anisotropic permeability tensors on nonorthogonal grids dictated by complex reservoir geology. Finite-difference, finite-volume, and (mixed) finite-element methods have all been used extensively in academia to solve the diffusion equation, but the cell-centered finite-volume method remains most popular among reservoir-simulation engineers because it has only one unknown per cell, is quite flexible for general grids, and uses the familiar principle of mass conservation. The simplest and currently most widely used finite-volume method is the linear two-point flux approximation (TPFA) where flux through a cell face is approximated by fluid pressure of the two neighboring cells that share the face (Aziz and Settari 1979). TPFA is quite robust and easy to implement, but is only consistent for the so-called K-orthogonal grids. To obtain a consistent discretization for general grids with arbitrary permeability tensors, linear multipoint flux approximation (MPFA) methods were proposed (Aavatsmark et al. 1996, 1998a, 1998b; Edwards and Rogers 1998; Aavatsmark 2002). The earlier MPFA methods are only conditionally monotone (Nordbotten and Aavatsmark 2005) and suffer from severe unphysical oscillations when the anisotropy ratio is high or the grid has large aspect ratios. MPFA methods with improved monotonicity properties were later addressed in Nordbotten and Eigestad (2005), Aavatsmark et al. (2008), Chen et al. (2008), Edwards and Zheng (2008, 2010), and Friis and Edwards (2011). Although these new MPFA methods can greatly reduce the unphysical oscillations, still they are not unconditionally monotone (Edwards 1995; Edwards and Rogers 1998) and it has been proved in Nordbotten et al. (2007) that a nine-point control volume scheme that satisfies local conservation and exact reproduction of linear solution while being unconditionally monotone is impossible.

Another class of finite-volume methods that are designed to be monotone is the cell-centered nonlinear method, which was originally proposed in Le Potier (2005). The nonlinear finite-volume method is formulated to preserve the positivity of the pressure solution and is therefore monotone. The price to pay is that a system of nonlinear equations needs to be solved even though the original problem is linear. The idea was further developed in Lipnikov et al. (2007, 2009, 2010), Yuan and Sheng (2008), Danilov and Vassilevski (2009), Queiroz et al. (2014), Wu and Gao (2014), Gao and Wu (2015), and Schneider et al. (2017b). A key ingredient of the method is to construct two one-sided fluxes for each internal grid face and a unique flux through the face is obtained by a convex combination of the two one-sided fluxes in such a way that a nonlinear two-point flux stencil (NTPFA) results. Although these nonlinear methods are monotone, they can still violate the discrete maximum/minimum principle (DMP). To preserve the extremum principle, a different convex combination of the one-sided fluxes was designed in Le Potier (2009), Sheng and Yuan (2011), Lipnikov et al. (2012), Gao and Wu (2013), and Svyatskiy and Lipnikov (2017), leading to nonlinear multipoint flux (NMPFA) stencils. Construction of one-sided fluxes usually requires decomposing conormal vectors of grid faces, and some auxiliary points are introduced to approximate the pressure gradient. To obtain a pure cell-centered method, pressure at these auxiliary points must be interpolated by pressure at cell centers. To preserve monotonicity or DMP, both the decomposition of the conormal vectors and the weighting coefficients in the interpolation are required to be nonnegative. Grid vertices are an obvious choice as auxiliary points, but the design of an accurate interpolating algorithm with nonnegative weighting coefficients for grid vertices turns out to be a difficult task. A more attractive option is the so-called harmonic-averaging point first proposed in Agélas et al. (2009). There is one harmonic-averaging point associated with each grid face, and pressure at the point can be interpolated by pressure of the two neighboring cells only with nonnegative weighting coefficients.

Unfortunately, the harmonic-averaging point is not robust in the sense that for discontinuous and highly anisotropic permeability tensors on challenging grids, the harmonic-averaging point can lie anywhere on the plane containing the grid face, which can cause problems for the decomposition of conormal vectors during the construction of one-sided fluxes. Specifically, if all the harmonic-averaging points associated with faces of a cell do not form a convex hull that contains the cell centroid, it might not be possible to

Copyright © 2019 Society of Petroleum Engineers

Original SPE manuscript received for review 3 November 2018. Revised manuscript received for review 16 March 2019. Paper (SPE 195694) peer approved 20 March 2019.

decompose the conormal vectors with nonnegative coefficients only. In practice, decomposition of conormal vectors using harmonic-averaging points can easily run into difficulties for heterogeneous and anisotropic permeability tensors on distorted nonorthogonal grids. In light of the difficulties associated with the interpolation procedures, an interpolation-free nonlinear finite-volume method was proposed in Danilov and Vassilevski (2009) and Lipnikov et al. (2009, 2010), but the method can be applied only to grids where each cell can have at most one face across which permeability jumps. In Wu and Gao (2014) and Gao and Wu (2015), a novel nonlinear formulation was proposed that does not require that the weighting coefficients of interpolation or coefficients of conormal decomposition be nonnegative. As a result, any second-order accurate interpolation algorithm can be used directly without replacing the negative coefficients with positive ones. This formulation was further extended to model flow problems for highly complex corner-point grids (Schneider et al. 2018). However, to preserve the monotonicity of the pressure solution, the method still requires that the sum of all the coefficients of each conormal decomposition be positive. This requirement is incorporated as a constraint into an optimization problem in Schneider et al. (2018) to determine the conormal decomposition. For challenging cases, the resulting conormal decomposition might involve more vectors than the dimension of the grid (e.g., more than three vectors are needed to decompose a conormal vector in three dimensions), leading to larger stencils for one-sided fluxes. Moreover, the formulation cannot be easily extended to preserve DMP of the solution. Therefore, it is highly desirable to devise an interpolating scheme that retains the simplicity of harmonic-averaging points and yet is less sensitive to permeability discontinuity and grid distortion, which is the focus of this work. To address this challenge, we first present an alternative formula of harmonic-averaging points that will show more clearly a point's location on grid faces. On the basis of the new formula, a correction algorithm is proposed to modify those ill-placed harmonic-averaging points so that all the conormal vectors can be decomposed with nonnegative coefficients successfully. Numerical experiments are conducted to investigate the robustness and accuracy of the resulting NFVM. The rest of the paper is organized as follows: The mathematical model is introduced in the succeeding section. The details of the nonlinear finite-volume methods and harmonic-averaging points are described in the Numerical Model section. Results of the numerical tests including the convergence study, monotonicity study, and one field test case are given in the Numerical Experiment section. The concluding remarks are provided in the Conclusions section.

Mathematical Model

Consider the following diffusion equation on an open bounded polygonal/polyhedral domain $\Omega \subset R^{\dim}$, $\dim = 2$ or 3:

$$\begin{aligned} &-\nabla \cdot (\mathbf{K}\nabla p) = q \quad \text{in} \quad \Omega, \\ &p = g_D \quad \text{on} \quad \Gamma_D, \\ &-\mathbf{K}\nabla p \cdot \hat{\mathbf{n}} = g_N \quad \text{on} \quad \Gamma_N, \end{aligned} \qquad \ldots\ldots\ldots\

where $\mathbf{x}_i$ is the centroid of cell Ω_i and $H_{i\sigma}$ is the set of faces whose associated harmonic-averaging points are involved in the decomposition of $\mathbf{w}_{i\sigma}$. Note that $H_{i\sigma}$ is a subset of $\partial\Omega_i$ and $\alpha_{i\sigma,\sigma'}$ are the corresponding decomposing coefficients and are required to be nonnegative in order for the method to be monotone or extremum-preserving. **Fig. 1** gives an example of conormal decomposition in two dimensions. The extension to three dimensions is straightforward. For certain permeability distribution and mesh geometries, the set $H_{i\sigma}$ might not exist. Addressing this challenge is the focus of this work and will be detailed in later subsections. On the other hand, when $H_{i\sigma}$ does exist, it might not be unique and various linear combinations for Eq 5 are possible. The choice of linear combinations can influence the accuracy of the resulting NFVM, as is demonstrated in Schneider et al. (2018). In this work, the searching algorithm suggested in Danilov and Vassilevski (2009) will be used to determine the set $H_{i\sigma}$. This searching algorithm is relatively efficient and ensures that out of all the allowable combinations of vectors $(\mathbf{x}_{\sigma'}-\mathbf{x}_i)$ that can be used to decompose $\mathbf{w}_{i\sigma}$, the chosen combination will be closest to $\mathbf{w}_{i\sigma}$. Substituting Eq. 5 into Eq. 4, we have

$$f_\sigma^{(i)} = -\sum_{\sigma'\in H_{i\sigma}} \alpha_{i\sigma,\sigma'}(p_{\sigma'} - p_i), \quad \ldots\ldots\ldots\

$$\mu_{\sigma,i}=\frac{r_{\sigma,j}}{r_{\sigma,i}+r_{\sigma,j}},\quad \mu_{\sigma,j}=\frac{r_{\sigma,i}}{r_{\sigma,i}+r_{\sigma,j}}, \quad \ldots\ldots\ldots\

where $\overline{g}_N$ is the average of g_N on face σ and $|\sigma|$ denotes the area of the face. Substituting flux expressions—Eqs. 13, 18, and 19—into the mass-balance equation (Eq. 2), a system of nonlinear equations is obtained:

$$\mathbf{A}(\mathbf{p})\mathbf{p} = \mathbf{b}(\mathbf{p}), \quad \ldots\ldots\ldots\

$$\mathbf{y}_\sigma = \frac{\lambda_1 d_2 \mathbf{y}_1 + \lambda_2 d_1 \mathbf{y}_2 + d_1 d_2 (\gamma_1 - \gamma_2)}{\lambda_1 d_2 + \lambda_2 d_1}. \quad \ldots\ldots\ldots\

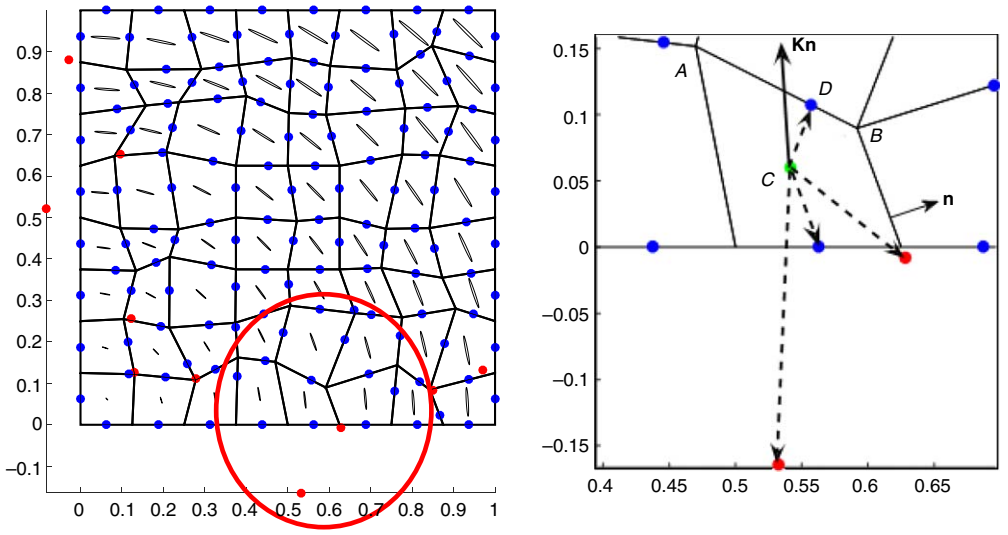

Fig. 4—Left: harmonic-averaging points (blue dots are harmonic-averaging points lying inside the face, and red dots are points lying outside the face). Right: zooming in on the circled part of the left plot.

Correction of the Harmonic-Averaging Point. Eq. 27 shows that if the two permeability tensors $\mathbf{K}_1$ and $\mathbf{K}_2$ are equal or they are isotropic, harmonic-averaging point $\mathbf{y}_\sigma$ will be bounded between the two projection points $\mathbf{y}_1$ and $\mathbf{y}_2$. To show more clearly the location of the harmonic-averaging point for general heterogeneous and anisotropic permeability tensors $\mathbf{K}_1$ and $\mathbf{K}_2$, we give a different derivation here. Still consider face σ shared by two cells shown in Fig. 3. First, we find the point $\mathbf{x}_A$ that lies on the plane containing face σ such that the vector $\mathbf{x}_A-\mathbf{x}_1$ is parallel to $\mathbf{K}_1\mathbf{n}_\sigma$. Similarly, we can find the point $\mathbf{x}_B$ such that vector $\mathbf{x}_B-\mathbf{x}_2$ is parallel to $-\mathbf{K}_2\mathbf{n}_\sigma$. Assuming that pressure unknown p is piecewise affine, flux out of cell Ω_1 and Ω_2 can be expressed individually as

$$f_\sigma^{(1)}=-(\nabla p)_1\cdot\mathbf{K}_1\mathbf{n}_\sigma|\sigma|\approx|\sigma|\frac{\|\mathbf{K}_1\mathbf{n}_\sigma\|}{\|\mathbf{x}_A-\mathbf{x}_1\|}(p_1-p_A)=|\sigma|\frac{w_1}{l_1}(p_1-p_A),$$
$$f_\sigma^{(2)}=-(\nabla p)_2\cdot(-\mathbf{K}_2\mathbf{n}_\sigma)|\sigma|\approx|\sigma|\frac{\|\mathbf{K}_2\mathbf{n}_\sigma\|}{\|\mathbf{x}_B-\mathbf{x}_2\|}(p_2-p_B)=|\sigma|\frac{w_2}{l_2}(p_2-p_B),\quad\ldots\ldots\ldots

By substituting Eq. 36 into Eqs. 34 and 35, Eqs. 27 and 28 can be recovered with some algebraic manipulations. Eq. 34 shows clearly that the harmonic-averaging point is bounded between the two points $\mathbf{x}_A$ and $\mathbf{x}_B$. Note that the above derivation applies to 3D space equally well.

Recall from Fig. 4 that the difficulty of decomposing conormal vectors with nonnegative coefficients is usually caused by those harmonic-averaging points that lie far outside their associated faces; we propose to improve the robustness of conormal decomposition by restricting the interpolating point to lie within a prescribed distance from the face centroid. For each harmonic-averaging point $\mathbf{y}_\sigma$, we define a ratio r_σ to quantify the extent to which $\mathbf{y}_\sigma$ deviates from the face centroid $\mathbf{x}_f$:

$$r_\sigma = \|\mathbf{y}_\sigma - \mathbf{x}_f\|/R, \quad \ldots\ldots (37)$$

where R is an equivalent radius of the face defined as $R = 0.5A$ in two dimensions and $R = \sqrt{A/\pi}$ in three dimensions, and A is the length of the face in two dimensions or area of the face in three dimensions. Now, we want to restrict the interpolating point to lie within a distance R' from the face centroid $\mathbf{x}_f$ (see **Fig. 5).** If $||\mathbf{y}_\sigma - \mathbf{x}_f|| \le R'$, the original harmonic averaging point $\mathbf{y}_\sigma$ can be used directly. However, if $||\mathbf{y}_\sigma - \mathbf{x}_f|| > R'$, a different point $\mathbf{y}_s$ is chosen as the new interpolating point. From our derivation of the harmonic-averaging point, we know that pressure of an arbitrary point $\mathbf{y}$ that lies on the plane containing the face is given by Eq. 33. However, pressure gradient $\mathbf{g}_\sigma$ along the plane containing σ is unknown and we cannot compute pressure at $\mathbf{y}_s$ directly. To overcome this problem, we choose the point $\mathbf{y}_s$ that will minimize the absolute value of the last term in the numerator of Eq. 33 and then drop that term. Pressure at $\mathbf{y}_s$ is then interpolated by the exact same equation as Eq. 35; that is,

$$p(\mathbf{y}_s) = \frac{\dfrac{w_1}{l_1}p_1 + \dfrac{w_2}{l_2}p_2 - \mathbf{g}_\sigma \cdot \left[\dfrac{w_1}{l_1}(\mathbf{x}_A - \mathbf{y}_s) + \dfrac{w_2}{l_2}(\mathbf{x}_B - \mathbf{y}_s)\right]}{\dfrac{w_1}{l_1} + \dfrac{w_2}{l_2}} \approx \frac{\dfrac{w_1}{l_1}p_1 + \dfrac{w_2}{l_2}p_2}{\dfrac{w_1}{l_1} + \dfrac{w_2}{l_2}}. \quad \ldots\ldots (38)$$

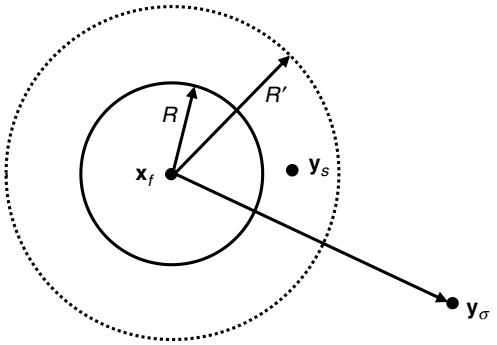

Fig. 5—Harmonic-averaging point $\mathbf{y}_\sigma$ lies far away from the centroid $\mathbf{x}_f$ of its associated face. A different point $\mathbf{y}_s$ within the specified radius R' is chosen as the new interpolating point.

Because we are using the same interpolation of pressure for $\mathbf{y}_\sigma$ and $\mathbf{y}_s$, $\mathbf{y}_s$ can be seen as a correction to the location of $\mathbf{y}_\sigma$. Dropping the last term runs the risk of losing accuracy, and a minimization problem is solved to keep the effect of the correction as small as possible. Because $\mathbf{g}_\sigma$ is unknown and noting that $\mathbf{g}_\sigma$ is parallel to the plane containing the face, we take $\mathbf{y}_s$ as the solution to the following optimization problem:

$$\text{Minimize } F(\mathbf{y}) = \left\|\frac{w_1}{l_1}(\mathbf{x}_A - \mathbf{y}) + \frac{w_2}{l_2}(\mathbf{x}_B - \mathbf{y})\right\|, \quad \ldots\ldots (39)$$

$$\text{subject to } \|\mathbf{y} - \mathbf{x}_f\| \le R'. \quad \ldots\ldots (40)$$

Upon solving the above optimization problem, $\mathbf{y}_s$ will be the new interpolating point for face σ and pressure interpolation at $\mathbf{y}_s$ is given by Eq. 38. For both 2D and 3D problems, the above optimization problem can be solved analytically (see Appendix A). For faces $\sigma \in \mathcal{F}_B^N$, our new interpolating point introduced in the preceding subsection can also deviate far from the face centroid and therefore might need correction as well. Assuming a constant pressure gradient $\mathbf{g}_\sigma$ along the plane containing σ, pressure at any point $\mathbf{y}$ on the plane can be calculated as

$$p(\mathbf{y}) = p_\sigma + (\mathbf{y} - \mathbf{y}_\sigma) \cdot \mathbf{g}_\sigma, \quad \ldots\ldots (41)$$

where p_σ is defined by Eq. 30. A new point $\mathbf{y}_s$ can be chosen to minimize $||\mathbf{y} - \mathbf{y}_\sigma||$. Pressure at $\mathbf{y}_s$ is then approximated by dropping the second term in Eq. 41. For faces $\sigma \in \mathcal{F}_B^D$, the face centroid is taken as the interpolating point and no correction is needed.

To investigate the effect of our correction algorithm on the accuracy of the respective NFVMs, we take a numerical test example from (Schneider et al. 2017b) and conduct a numerical convergence test by solving Eq. 1 using NTPFA and NMPFA. The computational domain is $\Omega = (-1, 1)^2$ and is composed of three subdomains, as shown in the left of **Fig. 6.** Permeability is isotropic in Subdomain 1 and 3 and anisotropic in Subdomain 2 with $k_1 = 1$, $k_3 = 100$, and $\mathbf{K}_2 = \text{diag}(10, k_{2y})$. We test the two cases where $k_{2y} = 10^3$ and 10^5, respectively. Ω is meshed by meshes that honor the internal permeability discontinuity. An example grid is shown in the right of Fig. 6. The mesh is refined consecutively by an $n \times n$ grid where $n = 8$, 16, 32, 64, and 128. The analytical pressure solution in each subdomain is given in polar coordinates as

$$p(r, \theta) = c + r^\alpha[a_i \cos(\alpha\theta) + b_i \sin(\alpha\theta)],\ i = 1, 2, 3, \quad \ldots\ldots (42)$$

where c is a constant to make sure the pressure solution stays positive. The other constants a_i and b_i are calculated by enforcing pressure and flux continuity across subdomain boundaries. Their exact values can be found in Schneider et al. (2017b). For this example, decomposition of conormal vectors with nonnegative coefficients can succeed without any correction to the original harmonic-averaging points despite the fact that some harmonic-averaging points associated with faces lying on the internal boundary between the subdomains lie outside their associated faces. Therefore, this example can be used to evaluate the possible loss of accuracy we might incur because of the corrections we made to the harmonic-averaging points. **Fig. 7** depicts the locations of harmonic-averaging points corrected by our correction algorithm with various R' values for each face on an 8×8 grid with $k_{2y} = 10^5$. The blue dots denote harmonic-averaging points lying inside their associated faces, and red dots denote harmonic-averaging points lying outside. In plot (a) of the figure, $R' = \infty$, meaning that no correction is made to any harmonic-averaging point. It can be seen that as R' decreases, those harmonic-averaging points lying far from their associated faces are gradually brought back to the faces. When $R' = R$, any harmonic-averaging point lying outside its associated face is corrected to lie on the face. **Figs. 8 and 9** show the convergence plots of pressure and flux solutions of NTPFA and NMPFA with various R' values for the two cases, respectively. A smaller value of R' means a larger degree of correction. The discrete L^2 norm of pressure and flux solutions is computed by Eq. 43 and is plotted against the inverse of mesh size h, which is computed as the mean of all face areas in a mesh. The classical multipoint flux approximation O (MPFA-O) method is used as a benchmark to evaluate the convergence behaviors of the two nonlinear methods. The results demonstrate that for this particular example, our correction algorithm actually has a positive effect on the accuracy of pressure solutions and the optimal convergence rate is still maintained after correction of harmonic-averaging points. The larger the degree of correction, the smaller the discrete pressure error norm. However, the convergence rate of flux solutions deteriorates for corrected harmonic-averaging points compared with the original harmonic-averaging points. This is especially true for the high-anisotropy case ($k_{2y} = 10^5$). Therefore, we propose to make corrections only when there exists a conormal that cannot be decomposed with nonnegative coefficients. This happens when there exists a cell whose centroid lies outside the convex hull of the harmonic-averaging points associated with its faces. Hence, we apply the above corrections to the involved harmonic-averaging points for such a cell. Out of all the harmonic-averaging points involved for the cell, we apply the corrections to the point $\mathbf{y}_\sigma$ that has the largest value of r_σ with a given value of R'. The corrections are applied recursively until the centroid of the cell lies inside the convex hull of the interpolating points associated with its faces. Therefore, the following correction algorithm is proposed.

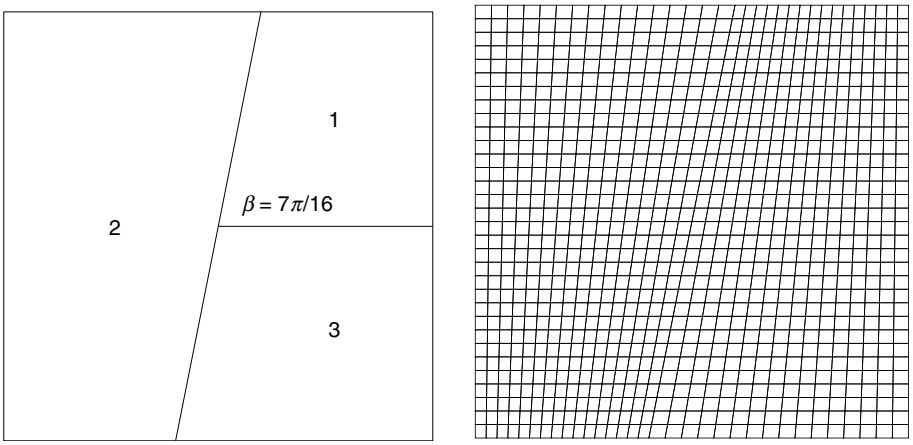

Fig. 6—Left: computational domain Ω composed of three regions with discontinuous permeability distributions; right: mesh conforming to internal permeability discontinuity.

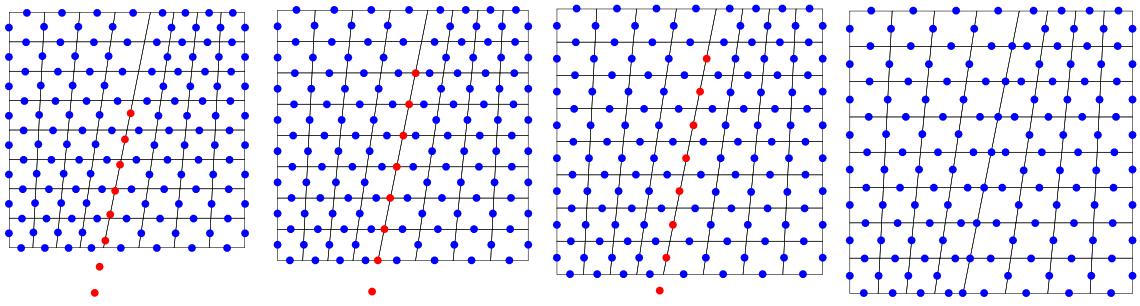

Fig. 7—Harmonic-averaging points with different R' values when $k_{2y} = 10^5$: (a) $R' =$ inf, (b) $R' = 3R$, (c) $R' = 2R$, (d) $R' = R$.

Step 1: Compute the locations of the original harmonic-averaging points using Eq. 34 and find the weighting coefficients using Eq. 35 for internal faces. For boundary faces, face centroid is taken as its harmonic-averaging point if the Dirichlet boundary condition is applied; when the Neumann boundary condition is specified on the boundary face, we use the strategy introduced in the Harmonic Averaging Point subsection and Eq. 30 to determine the harmonic-averaging point and its pressure reconstruction.

Step 2: Loop over all the cells in the grid to check for each cell whether its centroid lies within the convex hull of the harmonic-averaging points associated with its faces. If no cell violates this condition, go to Step 4; else, go to the next step.

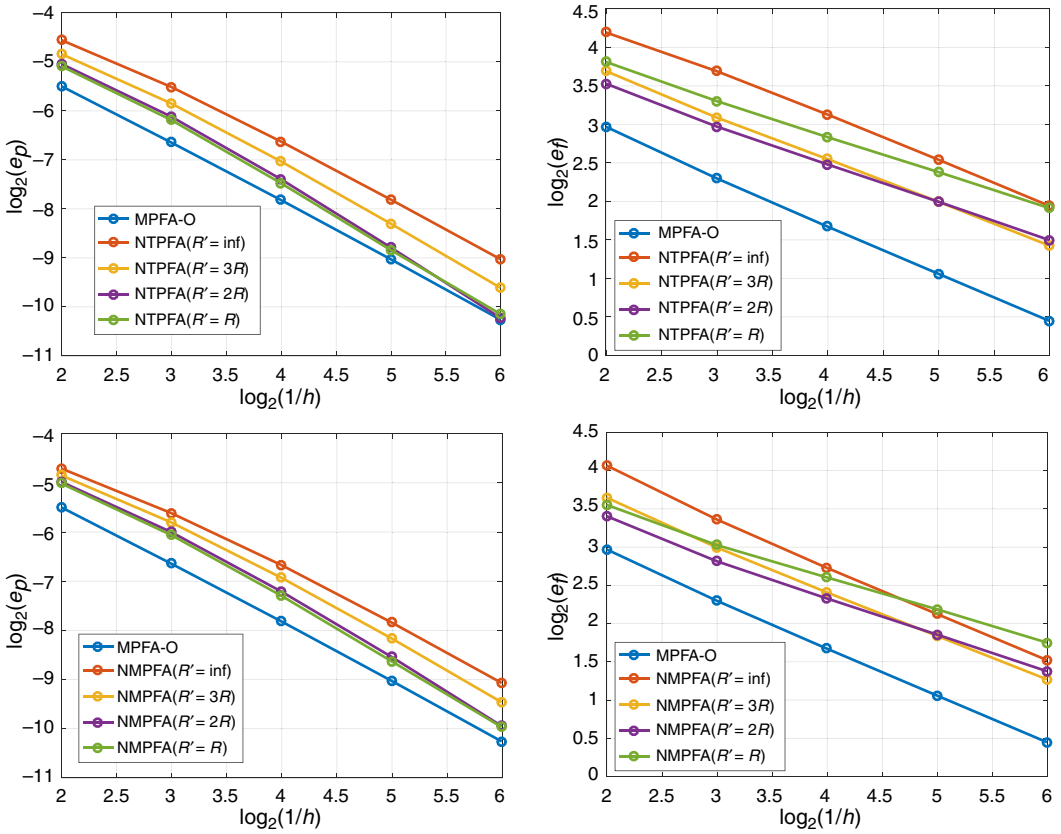

Fig. 8—Discrete L^2 norm of pressure errors (left column) and flux errors (right column) using NTPFA (first row) and NMPFA (second row) with various R' values for when $k_{2y} = 10^3$.

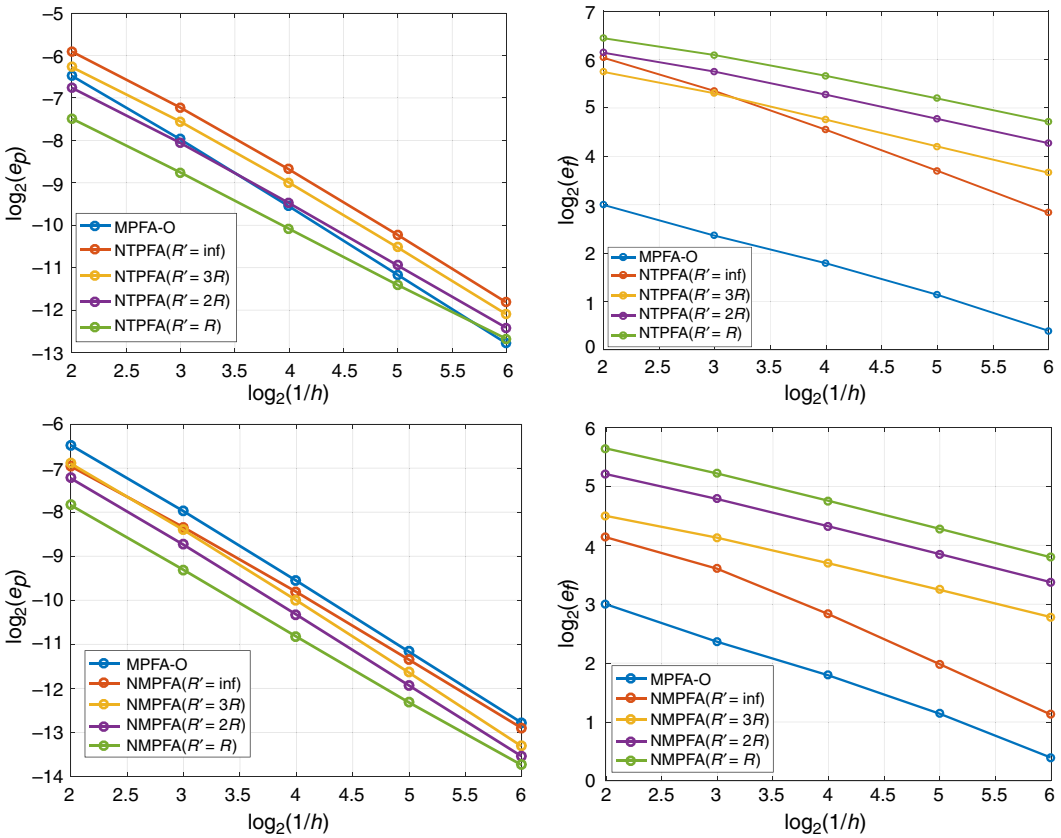

Fig. 9—Discrete L^2 norm of pressure errors (left column) and flux errors (right column) using NTPFA (first row) and NMPFA (second row) with various R' values when $k_{2y} = 10^5$.

Step 3: For the cell whose centroid lies outside the convex hull of the harmonic-averaging points associated with its faces, compute r_σ for each involved harmonic-averaging point and then sort all the r_σ values from largest to smallest and find the harmonic-averaging point $\mathbf{y}_{\sigma'}$ with the largest r_σ value denoted as $r_{\sigma_\max}$. Apply the correction using Eqs. 38 through 41 to this $\mathbf{y}_{\sigma'}$ depending on whether it lies on an internal face or a boundary face by taking $R' = \beta \cdot r_{\sigma_\max} \cdot R$ where β is a contracting factor satisfying $0 < \beta < 1$. A smaller value of β means a larger degree of correction to the location of $\mathbf{y}_{\sigma'}$. In our code, β is set to be 0.9. Then return to Step 2.

Step 4: Exit the algorithm.

The above algorithm is guaranteed to converge as long as the mesh and permeability distribution satisfy the requirement that for all the cells of the mesh, and the cell centroid lies inside the convex hull formed by all the centroids of its faces.

Numerical Experiments

Convergence Tests. In this subsection, numerical examples are presented to test the effect of our correction algorithm on the convergence behavior of the NFVMs. The MPFA-O method is used as a benchmark. The details of the MPFA-O method can be found in Aavatsmark (2002), and its convergence behavior was numerically tested in Eigestad and Klausen (2005). We implemented the MPFA-O method and the NFVMs within the framework of the open-source MATLAB reservoir simulation toolbox (MRST) (Lie et al. 2012). Our implementation of Dirichlet boundary conditions for the MPFA-O method follows the technique presented in Eigestad and Klausen (2005), and we validated our code with their published numerical results. The discrete L^2 norm defined by the following equations is used to quantify the error of pressure and flux solutions:

$$e_p = \|p - p_h\|_{L^2} = \left\{ \sum_i [A_i (p_i - p_{h,i})^2] \Big/ \sum_i A_i \right\}^{1/2},$$
$$e_f = \|f - f_h\|_{L^2} = \left(\sum_i \left\{ Q_{ei} [(f_i - f_{h,i})/e_i]^2 \right\} \Big/ \sum_i Q_{ei} \right)^{1/2}, \quad \ldots\ldots (43)$$

where p_i is the exact solution evaluated at the center of the ith control volume and $p_{h,i}$ is the corresponding numerical solution; A_i is the area/volume of the ith control volume. f_i is the flux across interface i using the exact solution evaluated at the centroid of the face, and $f_{h,i}$ is the corresponding numeral flux; e_i is the length/area of interface i and Q_{ei} is the area/volume associated with interface i, taking Q_{ei} as the half of the sum of two neighboring control volumes. The order of convergence of pressure solution R_p between two levels of mesh refinement is calculated by the following equation:

$$R_p = -\dim \frac{\ln[e_p(i)] - \ln[e_p(i-1)]}{\ln[n_c(i)] - \ln[n_c(i-1)]}, \quad \ldots\ldots (44)$$

where dim equals the dimension (2 or 3) of the problem, and n_c is the number of cells of the mesh. Convergence order of flux solutions R_f is calculated similarly with e_f replacing e_p in Eq. 44.

2D Tests. This example is taken from the 2D benchmark test of discretization schemes for anisotropic diffusion equations (Herbin and Hubert 2008). The permeability tensor is anisotropic, and the principal direction rotates smoothly throughout the domain. Its distribution is given by the following expression:

$$\mathbf{K} = \frac{1}{x^2 + y^2} \begin{bmatrix} y^2 + \varepsilon x^2 & -(1-\varepsilon)xy \\ -(1-\varepsilon)xy & \varepsilon y^2 + x^2 \end{bmatrix}. \quad \ldots\ldots (45)$$

The parameter ε in Eq. 45 is a constant that controls the strength of anisotropy of the permeability tensor. The computational domain is the unit square $\Omega = (0, 1)^2$. The analytical pressure solution is $p(x,y) = \sin(\pi x)\sin(\pi y) + 1$, and the source term is given by $q = -\nabla \cdot (\mathbf{K}\nabla p)$. The boundary condition is of Dirichlet type, $\Gamma_D = \partial\Omega$, with g_D given by the exact solution. The computational domain is discretized by randomly perturbed quadrilateral and acute-triangular meshes. **Fig. 10** shows an example of the two types of meshes. In our code, the permeability tensor is computed at the centroid of each cell and is piecewise constant as in Terekhov et al. (2017). This example is quite challenging because of both heterogeneity and anisotropy combined with nonorthogonal meshes. Note that in Herbin and Hubert (2008) the computational domain is discretized by uniform square meshes for which all the harmonic-averaging points lie inside their associated faces. **Fig. 11** shows the locations of the harmonic-averaging points before and after correction on a randomly perturbed 8×8 quadrilateral mesh when the anisotropy ratio is 1,000. It can be seen that a slight perturbation of the mesh leads to some harmonic-averaging points lying far outside their associated faces, as indicated by the red dots in the left plot. If the original harmonic-averaging points are used as interpolating points, decomposition of conormal vectors with nonnegative coefficients can easily fail on the nonorthogonal meshes used here. The right plot in the figure shows the locations of the harmonic-averaging points after our correction algorithm is applied. Those problematic harmonic-averaging points (black circles in the plots) are identified to cause the decomposition of some conormals to fail, and their locations are modified accordingly. **Fig. 12** further shows the convex hull of the associated harmonic-averaging points before and after our correction algorithm is applied for a quadrilateral and triangular cell in detail.

We first take the anisotropy ratio as 10 ($\varepsilon = 10^{-1}$). For this mild anisotropy ratio, no corrections are needed for the harmonic-averaging points because all the cell centroids lie inside the convex hull formed by their associated points. **Fig. 13** shows graphically the discrete L^2 norm of pressure and flux errors as a function of number of cells n_c on the two types of meshes for MPFA-O, NTPFA, and NMPFA methods. It can be seen that the three methods have comparable convergence behavior for both pressure and flux solutions. **Tables 1 and 2** list the discrete error norms, convergence rate at each mesh refinement level for the three methods, and the number of Picard iterations n_{iter} for the two nonlinear methods on quadrilateral and triangular meshes. The order of convergence of pressure solution is approximately second order and for flux solutions is first order. In general, more Picard iterations are needed for the two nonlinear methods as the mesh is refined. We also note that the number of Picard iterations for NMPFA reaches 500 for several meshes (marked in bold in Table 2) without converging to the specified stopping criterion although its effect on the final solution seems to be insignificant. Increasing the number of Picard iterations does not help because the norm of residuals fluctuates around a horizontal line, as depicted in **Fig. 14.** Because no correction is applied to the harmonic-averaging points in this case, this convergence issue with NMPFA is not caused by our correction algorithm.

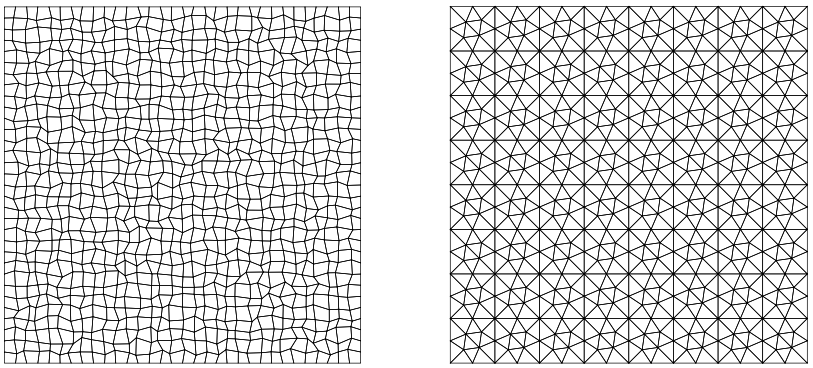

Fig. 10—Example of randomly perturbed quadrilateral mesh (left) and acute-triangular mesh (right).

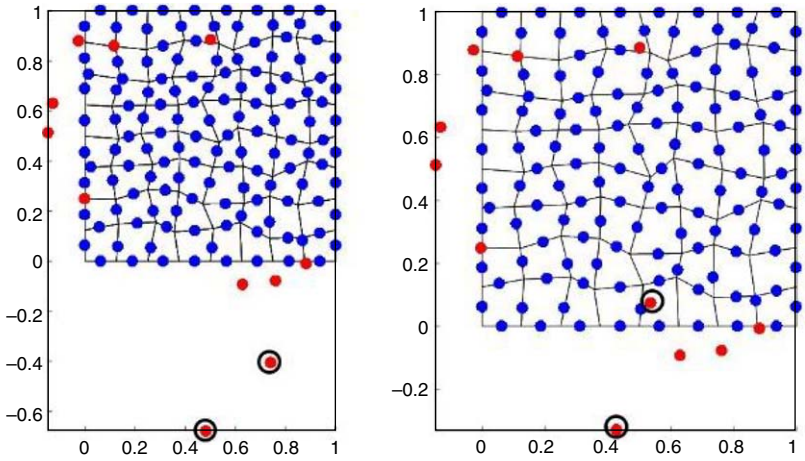

Fig. 11—Locations of harmonic-averaging points on a random quadrilateral mesh before correction (left) and after correction (right). Blue dots denote the harmonic-averaging points lying inside their associated face, while red dots denote the points lying outside their associated face. Our correction algorithm identifies those problematic harmonic-averaging points (black circled) and modifies their locations.

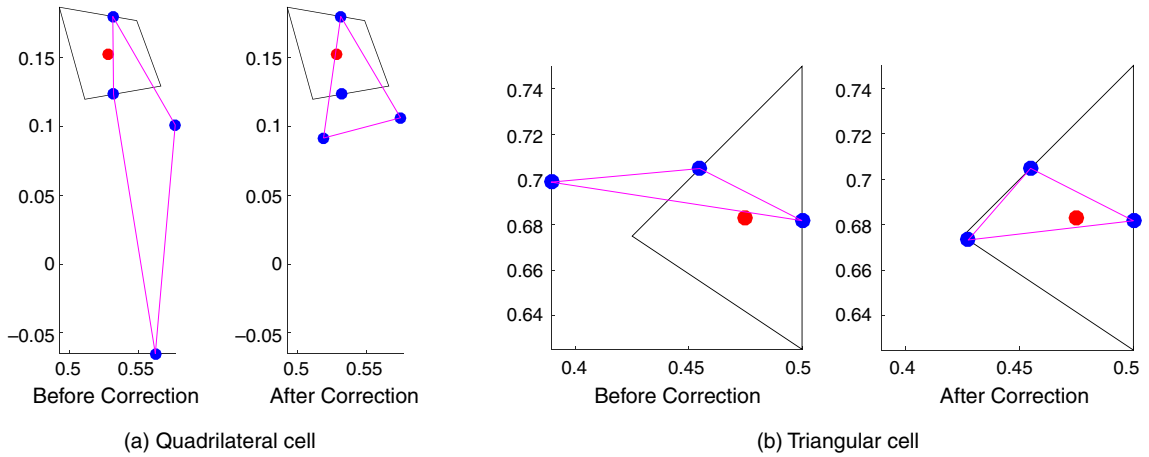

(a) Quadrilateral cell (b) Triangular cell

Fig. 12—Convex hull (magenta colored) formed by the harmonic-averaging points (blue dots) associated with a cell (black colored) before and after correction for a quadrilateral cell and a triangular cell. The cell centroid is denoted by the red dot: (a) quadrilateral cell and (b) triangular cell.

Next, we increase the anisotropy ratio to 1,000 and run the simulations again. **Table 3** lists the percentage of cells whose centroid lies outside the convex hull formed by its associated harmonic-averaging points before correction for each mesh. It can be seen that our correction algorithm needs to be applied for both quadrilateral and triangular meshes. This test case is also investigated in Schneider et al. (2017a) and Terekhov et al. (2017) on various meshes. The MPFA-O method is well-known to suffer from unphysical oscillations for highly anisotropic problems, and the convergence of MPFA-O is lost for this case as is pointed out in Terekhov et al. (2017). The

two nonlinear methods, on the other hand, still converge although at reduced orders, which is expected because of the high anisotropy ratio. Discrete error norms and orders of convergence at each mesh-refinement level for the three methods on random quadrilateral meshes and acute-triangular meshes are listed in **Tables 4 and 5,** respectively. On random quadrilateral meshes, compared to the relevant results presented in Schneider et al. (2017a), the order of convergence for NTPFA and NMPFA in this work shows only a slight deterioration that might be caused by our correction algorithm. However, on acute-triangular meshes, our NTPFA and NMPFA show performance comparable to the results presented in Terekhov et al. (2017) and the effect of our correction algorithm on the accuracy of NTPFA and NMPFA is minimal. Pressure solutions of both NTPFA and NMPFA converge at an approximate order of 1.5, and the first order of convergence is maintained for flux solutions. Also shown in Tables 4 and 5 are the number of Picard iterations for NTPFA and NMPFA on all the meshes. Similar to the previous case, NMPFA suffers from convergence issues for several meshes.

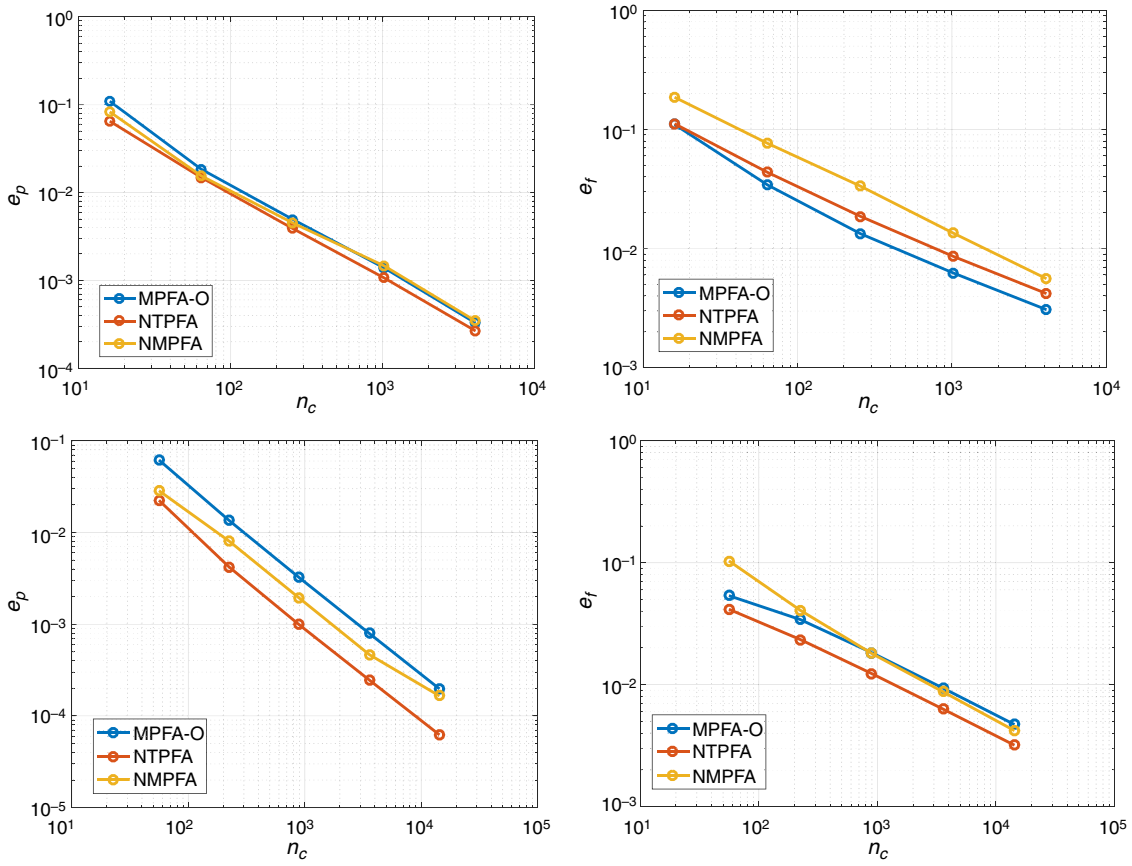

Fig. 13—L^2 norm of pressure (left column) and flux (right column) errors for the 2D convergence test of mild anisotropy on the random quadrilateral mesh (first row) and acute-triangular mesh (second row).

	MPFA-O				NTPFA					NMPFA				
n_c	e_p	R_p	e_f	R_f	e_p	R_p	e_f	R_f	n_{iter}	e_p	R_p	e_f	R_f	n_{iter}
64	2.37×10^{-2}	0	3.40×10^{-2}	0	1.37×10^{-2}	0	4.19×10^{-2}	0	23	1.93×10^{-2}	0	7.16×10^{-2}	0	42
256	5.35×10^{-3}	2.15	1.40×10^{-2}	1.27	3.65×10^{-3}	1.91	1.93×10^{-2}	1.12	39	5.20×10^{-3}	1.90	3.23×10^{-2}	1.15	54
1,024	1.29×10^{-3}	2.05	6.21×10^{-3}	1.18	1.03×10^{-3}	1.82	8.81×10^{-3}	1.13	52	1.31×10^{-3}	1.99	1.36×10^{-2}	1.24	70
4,096	3.37×10^{-4}	1.94	3.02×10^{-3}	1.04	2.76×10^{-4}	1.90	4.23×10^{-3}	1.06	64	3.26×10^{-4}	2.01	5.52×10^{-3}	1.30	86
16,384	8.41×10^{-5}	2.00	1.45×10^{-3}	1.05	7.40×10^{-5}	1.90	2.00×10^{-3}	1.08	72	8.52×10^{-5}	1.94	2.51×10^{-3}	1.14	95

Table 1—Results of 2D convergence test of mild anisotropy on random quadrilateral meshes.

	MPFA-O				NTPFA					NMPFA				
n_c	e_p	R_p	e_f	R_f	e_p	R_p	e_f	R_f	n_{iter}	e_p	R_p	e_f	R_f	n_{iter}
56	6.17×10^{-2}	0	5.36×10^{-2}	0	2.24×10^{-2}	0	4.15×10^{-2}	0	22	2.86×10^{-2}	0	1.03×10^{-1}	0	50
224	1.35×10^{-2}	2.19	3.42×10^{-2}	0.65	4.21×10^{-3}	2.41	2.34×10^{-2}	0.83	32	8.06×10^{-3}	1.82	4.07×10^{-2}	1.35	69
896	3.22×10^{-3}	2.07	1.83×10^{-2}	0.90	9.87×10^{-4}	2.09	1.23×10^{-2}	0.93	44	1.93×10^{-3}	2.06	1.80×10^{-2}	1.18	106
3,584	7.93×10^{-4}	2.02	9.35×10^{-3}	0.97	2.46×10^{-4}	2.00	6.30×10^{-3}	0.97	54	**4.66×10^{-4}**	**2.05**	**8.73×10^{-3}**	**1.05**	**500**
14,336	1.97×10^{-4}	2.01	4.71×10^{-3}	0.99	6.22×10^{-5}	1.98	3.18×10^{-3}	0.98	65	**1.65×10^{-4}**	**1.50**	**4.19×10^{-3}**	**1.06**	**500**

Table 2—Results of 2D convergence test of mild anisotropy on acute-triangular meshes.

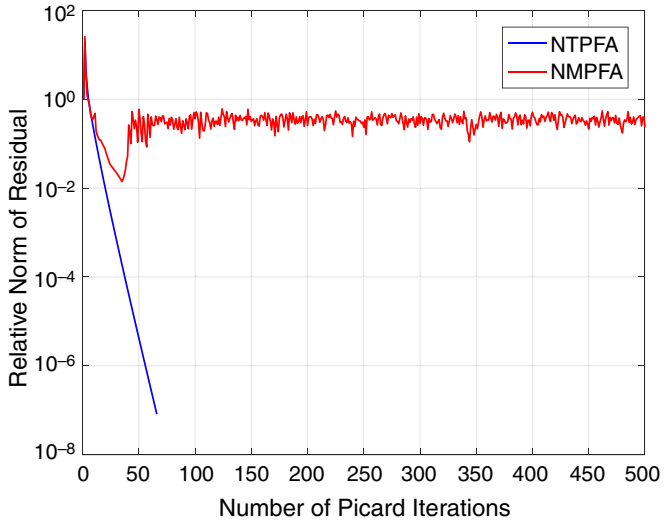

Fig. 14—Relative norm of residual during Picard nonlinear iterations for NTPFA and NMPFA on the acute-triangular mesh at the last refinement level.

Mesh-Refinement Level	Quadrilateral Mesh (%)	Triangular Mesh (%)
1	3.13	0
2	2.73	1.79
3	1.07	0.67
4	0.15	0.17
5	0.09	0.04

Table 3—Percentage of cells whose centroid lies outside the convex hull formed by its associated harmonic-averaging points on quadrilateral and triangular meshes at each mesh-refinement level for 2D convergence test of strong anisotropy.

	NTPFA					NMPFA				
n_c	e_p	R_p	e_f	R_f	n_{iter}	e_p	R_p	e_f	R_f	n_{iter}
64	4.56×10^{-2}	0.00	1.17×10^{-1}	0.00	32	5.73×10^{-2}	0.00	1.98×10^{-1}	0.00	71
256	1.37×10^{-2}	1.74	8.56×10^{-2}	0.45	67	**1.48×10^{-2}**	**1.95**	**1.30×10^{-1}**	**0.60**	**500**
1,024	1.16×10^{-2}	0.24	7.25×10^{-2}	0.24	141	**1.46×10^{-2}**	**0.02**	**8.05×10^{-2}**	**0.70**	**500**
4,096	3.58×10^{-3}	1.69	3.96×10^{-2}	0.87	259	**3.79×10^{-3}**	**1.95**	**4.69×10^{-2}**	**0.78**	**500**
16,384	1.16×10^{-3}	1.62	2.24×10^{-2}	0.82	473	**1.59×10^{-3}**	**1.26**	**2.80×10^{-2}**	**0.75**	**500**

Table 4—Results of 2D convergence test of strong anisotropy on random quadrilateral meshes.

	NTPFA					NMPFA				
n_c	e_p	R_p	e_f	R_f	n_{iter}	e_p	R_p	e_f	R_f	n_{iter}
56	4.41×10^{-2}	0	6.90×10^{-2}	0	29	5.61×10^{-2}	0	1.17×10^{-1}	0	102
224	1.29×10^{-2}	1.78	3.45×10^{-2}	1.00	56	2.17×10^{-2}	1.37	5.76×10^{-2}	1.04	111
896	5.57×10^{-3}	1.21	2.16×10^{-2}	0.68	111	1.02×10^{-2}	1.09	3.09×10^{-2}	0.90	256
3,584	1.87×10^{-3}	1.57	1.27×10^{-2}	0.77	211	4.01×10^{-3}	1.34	1.69×10^{-2}	0.87	439
14,336	5.39×10^{-4}	1.79	6.34×10^{-3}	1.00	395	**1.28×10^{-3}**	**1.64**	**8.39×10^{-3}**	**1.01**	**500**

Table 5—Results of 2D convergence test of strong anisotropy on acute-triangular meshes.

3D Tests. Case 1: Mild Anisotropy. This test case is taken from the 3D benchmark test of discretization schemes for anisotropic diffusion equations (Eymard et al. 2011) and features a constant permeability tensor with mild anisotropy,

$$\mathbf{K} = \begin{pmatrix} 1 & 0.5 & 0 \\ 0.5 & 1 & 0.5 \\ 0 & 0.5 & 1 \end{pmatrix}. \quad \ldots\ldots\ldots\

The analytical solution is given by $p(x,y,z) = 1 + \sin(\pi x)\sin[\pi(y + 1/2)]\sin[\pi(z + 1/3)]$. The Dirichlet condition is applied on the domain boundary. **Fig. 15** shows the meshes used in this example. The random hexahedral mesh is generated by randomly perturbing the vertices of a Cartesian mesh of the unit cube. Because of the random perturbation, the cell faces might not be planar in general and the computational domain is determined by the mesh. Face centroids, face normals, and face areas of the nonplanar faces are computed by the *computeGeometry* function provided in MRST, and details of calculation can be found in Lie (2014). The random perturbation is performed at each mesh-refinement level. The unstructured tetrahedral meshes are downloaded from the website of the 3D benchmark test (URL https://www.latp.univ-mrs.fr/latp_numerique/?q=node/11#mesh2). For the random hexahedral meshes, the original harmonic-averaging points can be successfully used for conormal decomposition and our correction algorithm does not need to be applied. For the unstructured tetrahedral meshes, the percentage of cells whose centroid is outside the convex hull of its associated harmonic-averaging points is 3.72, 5.64, 5.31, 4.11, and 5.06% for each level of mesh refinement, respectively. **Fig. 16** shows an example of a tetrahedral cell with its associated harmonic-averaging points. Before correction of the harmonic-averaging points, the cell centroid lies outside the convex hull and decomposition of conormals with nonnegative coefficients can fail for some of its faces. After correction, the cell centroid now lies inside the convex hull and all the conormals of this cell can be decomposed successfully with nonnegative coefficients. **Fig. 17** shows the convergence results of MPFA-O, NTPFA, and NMPFA graphically, and the corresponding order of convergence at each mesh-refinement level is listed in **Tables 6 and 7** on hexahedral and tetrahedral meshes, respectively. It can be seen that on random hexahedral meshes, the three methods have performance similar to that of MPFA-O, behaving slightly better than the two nonlinear methods. Pressure solutions converge at approximately second order, and flux solutions converge at higher than first order. Our results of nonlinear methods agree fairly well with those presented in Schneider et al. (2018) (the NTPFA is denoted by NLTPFA in their work). On tetrahedral meshes, the performance of NTPFA and NMPFA deteriorates, especially for the last mesh-refinement level. This test is also carried out in Wu and Gao (2014) on the same tetrahedral meshes. The method denoted by LPS-TP3 in their work uses harmonic-averaging points to decompose conormal vectors. However, because of conormal-decomposition issues, they presented results on meshes that correspond to mesh refinement Level 1–3 in this work and did not obtain results on finer meshes. Inspecting their available results reveals that the order of convergence for both pressure and flux solutions on the first three levels of mesh refinement is quite close between the two nonlinear methods in this work and their LPS-TP3 method, suggesting that the effect of our correction algorithm on the accuracy of the nonlinear methods is insignificant on these meshes. However, the lower performance on the last mesh-refinement level might be caused by our correction algorithm because more numbers of harmonic-averaging points need to be corrected.

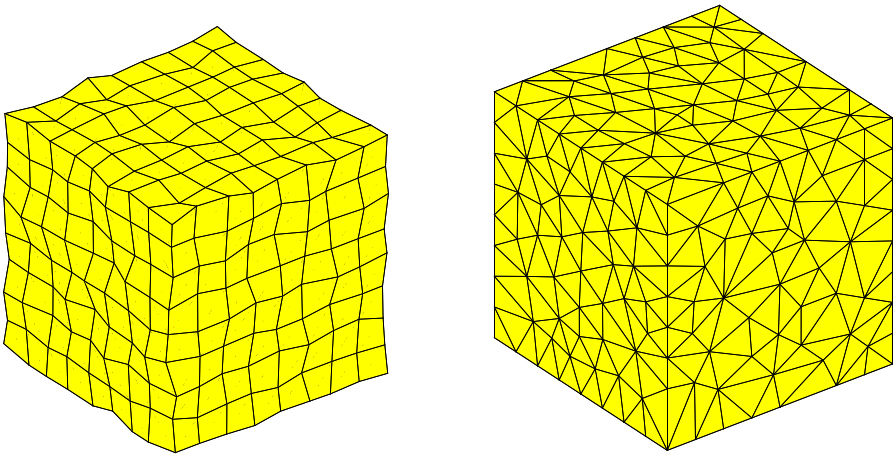

Fig. 15—Example of randomly perturbed hexahedral mesh (left) and unstructured tetrahedral mesh (right).

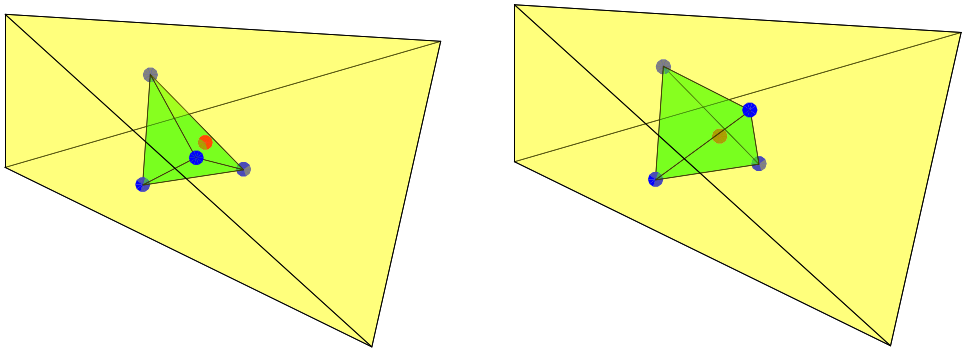

Fig. 16—Example of a tetrahedral cell (yellow-colored) and the convex hull (green-colored) of its associated harmonic-averaging points. The red dot is the centroid of the cell, and the blue dots are the harmonic-averaging points. Left: the cell centroid lies outside the convex hull of the original harmonic-averaging points; right: the same cell centroid lies inside the convex hull after our correction algorithm is applied to the harmonic-averaging points.

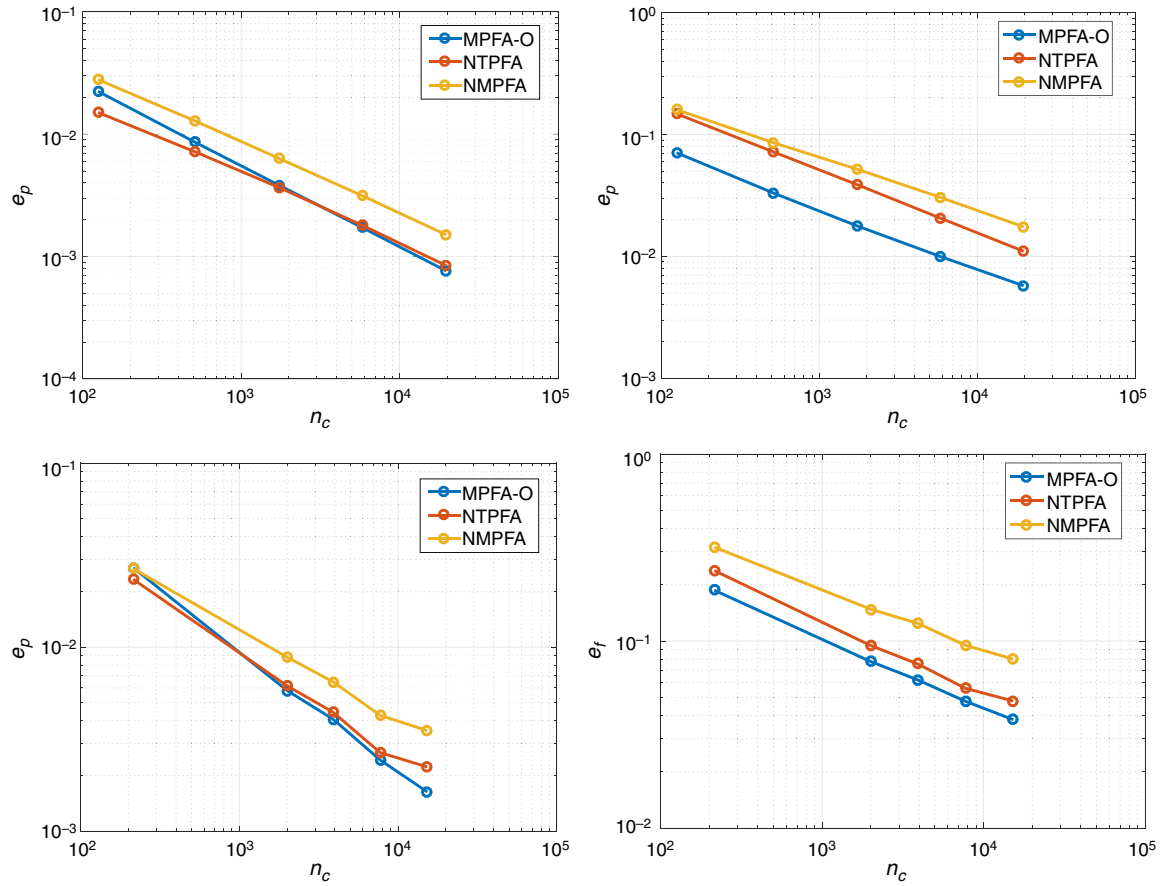

Fig. 17—L^2 norm of pressure (left column) and flux (right column) errors for 3D convergence test of mild anisotropy on random hexahedral mesh (first row) and unstructured triangular mesh (second row).

	MPFA-O				NTPFA					NMPFA				
n_c	e_p	R_p	e_f	R_f	e_p	R_p	e_f	R_f	n_{iter}	e_p	R_p	e_f	R_f	n_{iter}
125	2.24×10^{-2}	0	7.08×10^{-2}	0	1.51×10^{-2}	0	1.48×10^{-1}	0	19	2.80×10^{-2}	0	1.60×10^{-1}	0	23
512	8.61×10^{-3}	2.04	3.31×10^{-2}	1.62	7.18×10^{-3}	1.58	7.20×10^{-2}	1.53	26	1.28×10^{-2}	1.66	8.57×10^{-1}	1.32	32
1,728	3.84×10^{-3}	1.99	1.78×10^{-2}	1.53	3.68×10^{-3}	1.65	3.89×10^{-2}	1.52	30	6.36×10^{-3}	1.73	5.20×10^{-2}	1.23	39
5,832	1.72×10^{-3}	1.98	9.98×10^{-3}	1.43	1.80×10^{-3}	1.77	2.06×10^{-2}	1.56	34	**3.14×10^{-3}**	**1.74**	**3.05×10^{-2}**	**1.32**	**500**
19,683	7.63×10^{-4}	2.01	5.74×10^{-3}	1.36	8.43×10^{-4}	1.87	1.10×10^{-2}	1.55	33	1.51×10^{-3}	1.81	1.75×10^{-2}	1.38	66

Table 6—Results of 3D convergence test of mild anisotropy on random hexahedral meshes.

	MPFA-O				NTPFA					NMPFA				
n_c	e_p	R_p	e_f	R_f	e_p	R_p	e_f	R_f	n_{iter}	e_p	R_p	e_f	R_f	n_{iter}
215	2.71×10^{-2}	0	1.87×10^{-1}	0	2.34×10^{-2}	0	2.38×10^{-1}	0	33	2.67×10^{-2}	0	3.18×10^{-1}	0	60
2,003	5.81×10^{-3}	2.07	7.76×10^{-2}	1.18	6.16×10^{-3}	1.79	9.46×10^{-2}	1.24	38	**8.82×10^{-3}**	**1.49**	**1.48×10^{-1}**	**1.03**	**500**
3,898	4.06×10^{-3}	1.62	6.20×10^{-2}	1.01	4.43×10^{-3}	1.49	7.56×10^{-2}	1.01	42	**6.48×10^{-3}**	**1.39**	**1.25×10^{-1}**	**0.78**	**500**
7,711	2.44×10^{-3}	2.24	4.77×10^{-2}	1.16	2.67×10^{-3}	2.22	5.59×10^{-2}	1.32	51	**4.26×10^{-3}**	**1.84**	**9.49×10^{-2}**	**1.20**	**500**
15,266	1.63×10^{-3}	1.76	3.80×10^{-2}	1.00	2.23×10^{-3}	0.80	4.78×10^{-2}	0.69	40	**3.52×10^{-3}**	**0.84**	**8.01×10^{-2}**	**0.75**	**500**

Table 7—Results of 3D convergence test of mild anisotropy on unstructured tetrahedral meshes.

Case 2: Strong Anisotropy. This second case is also taken from Eymard et al. (2011) and deals with a constant tensor with strong anisotropy,

$$\mathbf{K} = \begin{pmatrix} 1 & 0 & 0 \\ 0 & 1 & 0 \\ 0 & 0 & 10^3 \end{pmatrix}. \quad \ldots\ldots\ldots\

Discrete error norms and order of convergence at each mesh refinement level for the two types of meshes are listed in **Tables 8 and 9,** respectively. On hexahedral meshes, the convergence order of pressure solutions for NTPFA approaches second order and flux solutions converge at higher than first order. The performance of NMPFA is lightly worse than for NTPFA. On tetrahedral meshes, the order of convergence for both NTPFA and NMPFA tends to be reduced in general. Pressure solutions converge at a similar rate for NTPFA and NMPFA, but NMPFA has lower order of convergence of flux solutions than NTPFA. To our knowledge, there are no published results of this test on tetrahedral meshes, which makes it difficult to assess to what degree the reduction of convergence order is caused by our correction algorithm and by the tetrahedral mesh itself.

	NTPFA					NMPFA				
n_c	e_p	R_p	e_f	R_f	n_{iter}	e_p	R_p	e_f	R_f	n_{iter}
125	3.50×10^{-2}	0	1.39×10^{2}	0	16	5.41×10^{-2}	0	1.83×10^{2}	0	28
512	2.02×10^{-2}	1.17	8.07×10^{1}	1.16	25	4.01×10^{-2}	0.64	1.28×10^{2}	0.76	44
1,728	1.08×10^{-2}	1.54	4.24×10^{1}	1.59	41	2.43×10^{-2}	1.23	7.50×10^{1}	1.31	93
5,832	5.51×10^{-3}	1.66	2.35×10^{1}	1.46	62	**1.07×10^{-2}**	**2.02**	**3.70×10^{1}**	**1.74**	**500**
19,683	2.59×10^{-3}	1.87	1.26×10^{1}	1.54	92	**6.45×10^{-3}**	**1.23**	**2.42×10^{1}**	**1.05**	**500**

Table 8—Results of 3D convergence test of strong anisotropy on random hexahedral meshes.

	NTPFA					NMPFA				
n_c	e_p	R_p	e_f	R_f	n_{iter}	e_p	R_p	e_f	R_f	n_{iter}
215	1.18×10^{-1}	0	4.86×10^{2}	0	51	1.34×10^{-1}	0	5.88×10^{2}	0	79
2,003	4.51×10^{-2}	1.29	2.27×10^{2}	1.02	90	**6.96×10^{-2}**	**0.88**	**3.76×10^{2}**	**0.60**	**500**
3,898	3.43×10^{-2}	1.23	1.79×10^{2}	1.08	98	**4.87×10^{-2}**	**1.61**	**2.82×10^{2}**	**1.29**	**500**
7,711	2.84×10^{-2}	0.84	1.41×10^{2}	1.07	126	**3.94×10^{-2}**	**0.93**	**2.38×10^{2}**	**0.76**	**500**
15,266	2.12×10^{-2}	1.27	1.12×10^{2}	0.98	156	**2.93×10^{-2}**	**1.31**	**1.97×10^{2}**	**0.82**	**500**

Table 9—Results of 3D convergence test of strong anisotropy on unstructured tetrahedral meshes.

No-Flow Boundary Condition. Monotonicity properties of NFVMs have been tested extensively in the literature. The property of positive-preserving or extremum-preserving can be proved mathematically from the formulation of the respective NFVM. Therefore, in this subsection, we include only one example to test the performance of the nonlinear methods on domains with no-flow boundary conditions. Calculation of interpolating points of faces lying on no-flow boundaries is introduced in the Harmonic-Averaging Point subsection. The example is taken from Aavatsmark et al. 2008 and is used to investigate the DMP for no-flow boundary conditions. The unit square domain $(0, 1)^2$ is meshed by an 11×11 Cartesian grid. Permeability is given by the following formula:

$$\mathbf{K} = \begin{bmatrix} \cos\theta & -\sin\theta \\ \sin\theta & \cos\theta \end{bmatrix} \begin{bmatrix} 1000 & 0 \\ 0 & 1 \end{bmatrix} \begin{bmatrix} \cos\theta & \sin\theta \\ -\sin\theta & \cos\theta \end{bmatrix}, \quad \ldots\ldots\ldots\

the focus of this work is to solve the diffusion equation, we keep the physics simple. Both fluid viscosity and density are assumed to be unity. No-flow boundary conditions are applied on all the boundary faces, as is often the case for reservoir-simulation problems. Therefore, harmonic-averaging points on boundary faces are defined according to our new definition given in the Harmonic Averaging Point subsection. There are approximately 0.1% of cells whose centroid lies outside the convex hull of its associated harmonic-averaging points before correction. Therefore, application of our correction algorithm to the harmonic-averaging points is necessary. Fluid flow is driven by the two wells. Bottomhole pressure of the injection well and production well is fixed at 20 and 10 MPa, respectively. The source term in Eq. 1 is related to the wells by the Peaceman well model (Chen et al. 2006). For comparison, the model was simulated using the NTPFA method in this work and the standard linear TPFA method. The linear TPFA method is known to be inconsistent for the non-K-orthogonal grid and suffers from the grid-orientation effect. The NMPFA method, unfortunately, encounters convergence issues again using Picard iterations and its results will not be shown here. In comparison, the NTPFA method converges after 42 Picard iterations. For a reference solution, the classical MPFA-O method is not applicable for this model because it is unable to deal with grids consisting of arbitrary polyhedrons. Therefore, we used another consistent discretization called the mimetic finite-difference (MFD) method that is provided in MRST. The pressure solution of linear TPFA, NTPFA, and MFD are denoted as $\boldsymbol{p}_{\text{tpfa}}$, $\boldsymbol{p}_{\text{ntpfa}}$, and $\boldsymbol{p}_{\text{mfd}}$, respectively. **Fig. 21** shows the difference between $\boldsymbol{p}_{\text{tpfa}}$ and $\boldsymbol{p}_{\text{mfd}}$ as well as the difference between $\boldsymbol{p}_{\text{ntpfa}}$ and $\boldsymbol{p}_{\text{mfd}}$ in absolute values. The results show that the NTPFA method gives a much closer pressure solution to MFD compared with the linear TPFA method. To investigate the quality of flux solutions, the following passive tracer transport equation ignoring dispersion is solved once we have the flux solution (Sandve et al. 2012):

$$\frac{\partial(\phi c)}{\partial t}+\nabla\cdot(c\mathbf{v})=q_c, \quad \ldots\ldots\ldots\

where V_i is the volume of cell i and Δt is the timestep; c_i^{n+1} and c_i^n are concentration of tracer of cell i at the next time level and the current time level, respectively; $\mathbb{N}(i)$ is the index set of neighboring cells that share a common face with cell i; c_{ij}^{n+1} is tracer concentration on the interface between cell i and j; f_{ij} is flux flowing from cell i to j; and Q_{ci} is the integrated tracer source in cell i. The value of c_{ij}^{n+1} is equal to c_i^{n+1} or c_i^{n+1} depending on the sign of flux f_{ij}. We further assume that tracer concentration in the injection well is always unity, giving rise to constant tracer source terms for cells that are penetrated by the injection well. At the end of 1 PV injection after 100 timesteps, the differences in tracer concentration between linear TPFA and MFD and between NTPFA and MFD are shown in **Fig. 22.** It can be seen that the magnitude of differences between NTPFA and MFD is smaller than that between linear TPFA and MFD. Therefore, this example demonstrates that our correction algorithm can be applied to nonlinear methods to solve physically realistic problems.

	$p_{\min}$	$p_{\max}$	n_{iter}
MPFA-O	–0.0600	1.0600	\
NTPFA	0.0143	1.5263	171
NMPFA	0.0168	0.9724	99

Table 10—Computational results for DMP test on the domain with no-flow boundaries.

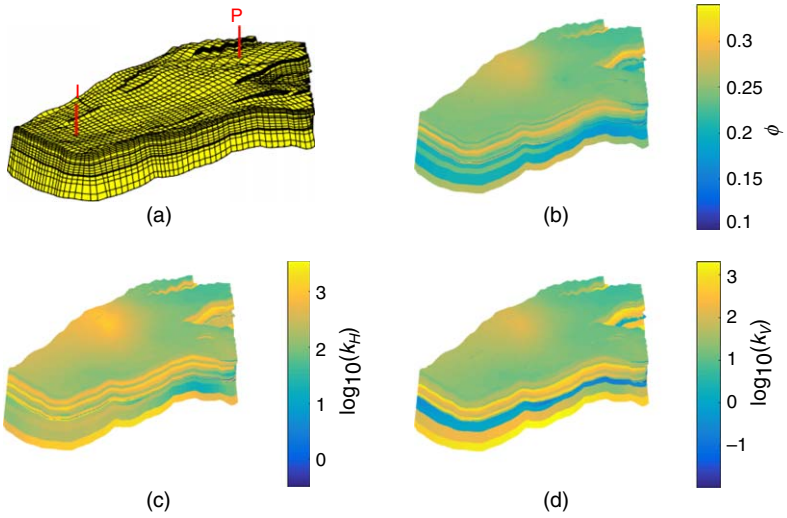

Fig. 20—Geological model of a field test case: (a) grid model (I = injector well, P = producer well); (b) porosity ϕ; (c) horizontal permeability k_H; (d) vertical permeability k_V.

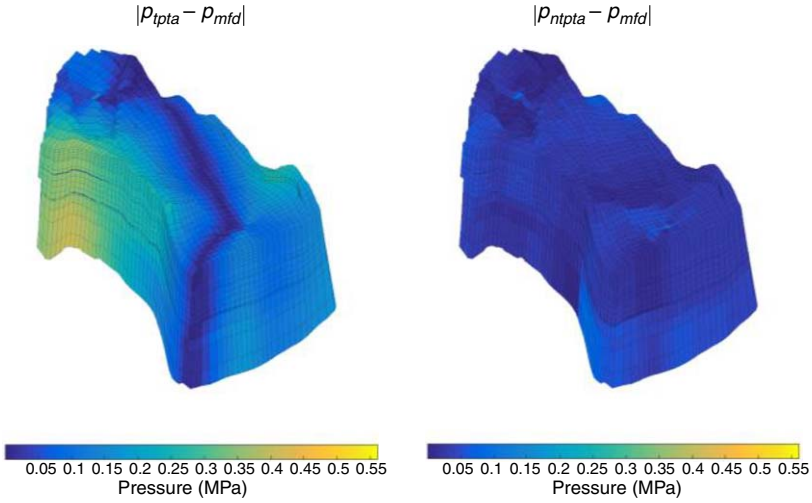

Fig. 21—Absolute-pressure difference between linear TPFA and MFD (left), and between NTPFA and MFD (right).

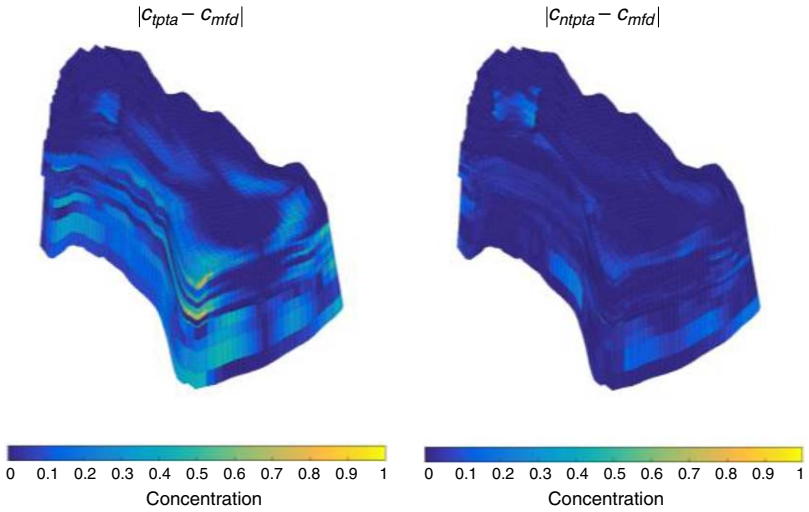

Fig. 22—Absolute-concentration difference between linear TPFA and MFD (left), and between NTPFA and MFD (right).

Conclusions

A cell-centered NFVM with improved robustness is presented in this paper. The NTPFA method is positivity-preserving, while the NMPFA is extremum-preserving. The concept of harmonic-averaging points is used for interpolation during the construction of one-sided fluxes. A correction algorithm is proposed to address the main drawback of harmonic-averaging points—namely, for heterogeneous and highly anisotropic permeability tensors on general nonorthogonal grids, a harmonic-averaging point can lie anywhere on the plane containing its associated face, causing potential problems for the decomposition of conormal vectors with nonnegative coefficients. By using the correction algorithm, the robustness of the nonlinear methods can be improved significantly. The correction algorithm is a compromise between robustness and accuracy. By solving a minimization problem, the negative effect on the accuracy of the scheme is kept minimal. Results of convergence in both 2D and 3D tests show that the optimal order of convergence is still maintained for some problems but the convergence rate is reduced for others. A monotonicity test on a domain with no-flow boundary conditions verified that both NTPFA and NMFPA methods preserve the positivity of pressure solutions but only NMPFA respects the discrete maximum principle, and our simple strategy of defining a new interpolating point on boundary faces with Neumann boundary conditions seems to work well, but more work is needed for more-robust handling of Neumann boundary conditions. Finally, the NTPFA method combined with our correction algorithm is applied to a field test case to demonstrate that it can be used to simulate flow in reservoirs of industry-standard complexity. However, our numerical experiments also reveal that the NMPFA method can suffer from convergence difficulties during Picard iterations for challenging problems.

Nomenclature

c = tracer concentration
$\mathrm{d}\mathbf{S}$ = oriented areal element
e_f = L^2 norm of flux errors
e_p = L^2 norm of pressure errors
f_σ = numerical flux through face σ
$\mathcal{F}$ = set of faces
$\mathcal{F}_B$ = set of boundary faces
$\mathcal{F}_I$ = set of internal faces
$\mathcal{F}_B^D$ = set of Dirichlet boundary faces
$\mathcal{F}_B^N$ = set of Neumann boundary faces
g_D = Dirichlet boundary condition
g_N = Neumann boundary condition
g_σ = pressure gradient along face σ
H = index set of faces involved in decomposition of conormal vector
$\mathbf{K}$ = permeability tensor
$\mathcal{M}$ = set of cells
$\hat{\mathbf{n}}$ = unit normal vector
p = pressure
q = fluid source term
q_c = tracer source term
R = equivalent radius
t = time
t_k = transmissibility of pressure at cell Ω_k
T = nonlinear transmissibility
w = weighting coefficient of harmonic averaging point
$\mathbf{w}$ = conormal vector
$\mathbf{x}$ = position vector
$\mathbf{y}_\sigma$ = harmonic averaging point associated with face σ
α = coefficient of conormal decomposition
β = contracting factor

Γ_D = Dirichlet boundary
Γ_N = Neumann boundary
μ = convex combination parameter
σ = generic face
φ = index set of cells involved in interpolating harmonic averaging point
ϕ = porosity
ψ_σ = index set of cells involved in approximating f_σ
$\partial\Omega$ = boundary of computation domain
Ω = computational domain
Ω_i = ith cell

References

Aavatsmark, I. 2002. An Introduction to Multipoint Flux Approximations for Quadrilateral Grids. *Comput Geosci* **6** (3–4): 405-432. https://doi.org/10.1023/A:1021291114475.

Aavatsmark, I., Barkve, T., Bøe, Ø. et al. 1996. Discretization on Non-Orthogonal, Quadrilateral Grids for Inhomogeneous, Anisotropic Media. *J Comput Phys* **127** (1): 2–14. https://doi.org/10.1006/jcph.1996.0154.

Aavatsmark, I., Barkve, T., Bøe, O. et al. 1998a. Discretization on Unstructured Grids for Inhomogeneous, Anisotropic Media. Part I: Derivation of the Methods. *SIAM J Sci Comput* **19** (5): 1700–1716. https://doi.org/10.1137/S1064827595293582.

Aavatsmark, I., Barkve, T., and Mannseth, T. 1998b. Control-Volume Discretization Methods for 3D Quadrilateral Grids in Inhomogeneous, Anisotropic Reservoirs. *SPE J.* **3** (2): 146–154. SPE-38000-PA. https://doi.org/10.2118/38000-PA.

Aavatsmark, I., Eigestad, G. T., Mallison, B. T. et al. 2008. A Compact Multipoint Flux Approximation Method With Improved Robustness. *Numer Methods Partial Differ Equ* **24** (5): 1329–1360. https://doi.org/10.1002/num.20320.

Agélas, L., Eymard, R., and Herbin, R. 2009. A Nine Point Finite Volume Scheme for the Simulation of Diffusion in Heterogeneous Media (in English). *Comptes rendus de l'Académie des sciences Série I, Mathématique* **347** (11–12): 673–676. https://hal.archives-ouvertes.fr/hal-00350139.

Aziz, K. and Settari, A. 1979. *Petroleum Reservoir Simulation*. Chapman & Hall.

Chen, Z., Huan, G., and Ma, Y. 2006. *Computational Methods for Multiphase Flows in Porous Media*. Philadelphia, Pennsylvania: Society for Industrial and Applied Mathematics.

Chen, Q.-Y., Wan, J., Yang, Y. et al. 2008. Enriched Multi-Point Flux Approximation for General Grids. *J Comput Phys* **227** (3): 1701–1721. https://doi.org/10.1016/j.jcp.2007.09.021.

Danilov, A. and Vassilevski, Y. V. 2009. A Monotone Nonlinear Finite Volume Method for Diffusion Equations on Conformal Polyhedral Meshes. *Russian J Numer Anal Math Modell* **24** (3): 207–227. https://doi.org/10.1007/s10596-013-9387-6.

Edwards, M. G. 1995. Symmetric Flux Continuous Positive Definite Approximation of the Elliptic Full Tensor Pressure Equation in Local Conservation Form. Presented at the SPE Reservoir Simulation Symposium, San Antonio, Texas, 1 January. SPE-29147-MS. https://doi.org/10.2118/29147-MS.

Edwards, M. G. and Rogers, C. F. 1998. Finite Volume Discretization With Imposed Flux Continuity for the General Tensor Pressure Equation. *Comput Geosci* **2** (4): 259–290. https://doi.org/10.1023/A:1011510505406.

Edwards, M. G. and Zheng, H. 2008. A Quasi-Positive Family of Continuous Darcy-Flux Finite-Volume Schemes With Full Pressure Support. *J Comput Phys* **227** (22): 9333–9364. https://doi.org/10.1016/j.jcp.2008.05.028.

Edwards, M. G. and Zheng, H. 2010. Double-Families of Quasi-Positive Darcy-Flux Approximations With Highly Anisotropic Tensors on Structured and Unstructured Grids. *J Comput Phys* **229** (3): 594–625. http://www.sciencedirect.com/science/article/pii/S0021999109005294.

Eigestad, G. and Klausen, R. 2005. On the Convergence of the Multi-Point Flux Approximation O-Method: Numerical Experiments for Discontinuous Permeability. *Numer Methods Partial Differ Equ Int J* **21** (6): 1079–1098. https://doi.org/10.1002/num.20079.

Eymard, R., Henry, G., Herbin, R. et al. 2011. 3D Benchmark on Discretization Schemes for Anisotropic Diffusion Problems on General Grids. In *Finite Volumes for Complex Applications VI Problems & Perspectives*, 895–930. Berlin, Heidelberg: Springer.

Friis, H. A. and Edwards, M. G. 2011. A Family of MPFA Finite-Volume Schemes With Full Pressure Support for the General Tensor Pressure Equation on Cell-Centered Triangular Grids. *J Comput Phys* **230** (1): 205–231. https://doi.org/10.1016/j.jcp.2010.09.012.

Gao, Z. and Wu, J. 2013. A Small Stencil and Extremum-Preserving Scheme for Anisotropic Diffusion Problems on Arbitrary 2D and 3D Meshes. *J Comput Phys* **250:** 308–331. https://doi.org/10.1016/j.jcp.2013.05.013.

Gao, Z. and Wu, J. 2015. A Second-Order Positivity-Preserving Finite Volume Scheme for Diffusion Equations on General Meshes. *SIAM J Sci Comput* **37** (1): A420–A438. https://doi.org/10.1137/140972470.

Herbin, R. and Hubert, F. 2008. Benchmark on Discretization Schemes for Anisotropic Diffusion Problems on General Grids. In *Finite Volumes for Complex Applications V*, 659–692. Wiley.

Le Potier, C. 2005. Schéma volumes finis monotone pour des opérateurs de diffusion fortement anisotropes sur des maillages de triangles non structurés. *Comptes Rendus Mathematique* **341** (12): 787–792. https://doi.org/10.1016/j.crma.2005.10.010.

Le Potier, C. 2009. A Nonlinear Finite Volume Scheme Satisfying Maximum and Minimum Principles for Diffusion Operators. *Int J Finite Vol*: 1–20.

Lie, K.-A. 2014. *An Introduction to Reservoir Simulation Using MATLAB: User Guide for the MATLAB Reservoir Simulation Toolbox (MRST)*. Norway: SINTEF ICT.

Lie, K. A., Krogstad, S., Ligaarden, I. S. et al. 2012. Open-Source MATLAB Implementation of Consistent Discretisations on Complex Grids. *Comput Geosci* **16** (2): 297–322. https://doi.org/10.1007/s10596-011-9244-4.

Lipnikov, K., Shashkov, M., Svyatskiy, D. et al. 2007. Monotone Finite Volume Schemes for Diffusion Equations on Unstructured Triangular and Shape-Regular Polygonal Meshes. *J Comput Phys* **227** (1): 492–512. https://doi.org/10.1016/j.jcp.2007.08.008.

Lipnikov, K., Svyatskiy, D., and Vassilevski, Y. 2009. Interpolation-Free Monotone Finite Volume Method for Diffusion Equations on Polygonal Meshes. *J Comput Phys* **228** (3): 703–716. https://doi.org/10.1016/j.jcp.2008.09.031.

Lipnikov, K., Svyatskiy, D., and Vassilevski, Y. 2010. A Monotone Finite Volume Method for Advection–Diffusion Equations on Unstructured Polygonal Meshes. *J Comput Phys* **229** (11): 4017–4032. https://doi.org/10.1016/j.jcp.2010.01.035.

Lipnikov, K., Svyatskiy, D., and Vassilevski, Y. 2012. Minimal Stencil Finite Volume Scheme With the Discrete Maximum Principle. *Russian J Numer Anal Math Modell* **27** (4): 369–386. https://doi.org/10.1515/rnam-2012-0020.

Nordbotten, J. M. and Aavatsmark, I. 2005. Monotonicity Conditions for Control Volume Methods on Uniform Parallelogram Grids in Homogeneous Media. *Comput Geosci* **9** (1): 61–72. https://doi.org/10.1007/s10596-005-5665-2.

Nordbotten, J. M., Aavatsmark, I., and Eigestad, G. T. 2007. Monotonicity of Control Volume Methods. *Numerische Mathematik* **106** (2): 255–288. https://doi.org/10.1007/s00211-006-0060-z.

Nordbotten, J. M. and Eigestad, G. T. 2005. Discretization on Quadrilateral Grids With Improved Monotonicity Properties. *J Comput Phys* **203** (2): 744–760. https://doi.org/10.1016/j.jcp.2004.10.002.

Queiroz, L., Souza, M., Contreras, F. et al. 2014. On the Accuracy of a Nonlinear Finite Volume Method for the Solution of Diffusion Problems Using Different Interpolations Strategies. *Int J Numer Methods Fluids* **74** (4): 270–291. https://doi.org/10.1002/fld.3850.

Sandve, T. H., Berre, I., and Nordbotten, J. M. 2012. An Efficient Multi-Point Flux Approximation Method for Discrete Fracture–Matrix Simulations. *J Comput Phys* **231** (9): 3784–3800. https://doi.org/10.1016/j.jcp.2012.01.023.

Schneider, M., Agélas, L., Enchéry, G. et al. 2017a. Convergence of Nonlinear Finite Volume Schemes for Heterogeneous Anisotropic Diffusion on General Meshes. *J Comput Phys* **351:** 80–107. https://doi.org/10.1016/j.jcp.2017.09.003.

Schneider, M., Flemisch, B., and Helmig, R. 2017b. Monotone Nonlinear Finite-Volume Method for Nonisothermal Two-Phase Two-Component Flow in Porous Media. *Int J Numer Methods Fluids* **84** (6): 352–381. https://doi.org/10.1002/fld.4352.

Schneider, M., Flemisch, B., Helmig, R. et al. 2018. Monotone Nonlinear Finite-Volume Method for Challenging Grids. *Comput Geosci*: 1–22. https://doi.org/10.1007/s10596-017-9710-8.

Sheng, Z. and Yuan, G. 2011. The Finite Volume Scheme Preserving Extremum Principle for Diffusion Equations on Polygonal Meshes. *J Comput Phys* **230** (7): 2588–2604. https://doi.org/10.1016/j.jcp.2010.12.037.

Svyatskiy, D. and Lipnikov, K. 2017. Second-Order Accurate Finite Volume Schemes With the Discrete Maximum Principle for Solving Richards' Equation on Unstructured Meshes. *Adv Water Resour* **104:** 114–126. https://doi.org/10.1016/j.advwatres.2017.03.015.

Terekhov, K. M., Mallison, B. T., and Tchelepi, H. A. 2017. Cell-Centered Nonlinear Finite-Volume Methods for the Heterogeneous Anisotropic Diffusion Problem. *J Comput Phys* **330:** 245–267. https://doi.org/10.1016/j.jcp.2016.11.010.

Wu, J. and Gao, Z. 2014. Interpolation-Based Second-Order Monotone Finite Volume Schemes for Anisotropic Diffusion Equations on General Grids. *J Comput Phys* **275:** 569–588. https://doi.org/10.1016/j.jcp.2014.07.011.

Yuan, G. and Sheng, Z. 2008. Monotone Finite Volume Schemes for Diffusion Equations on Polygonal Meshes. *J Comput Phys* **227** (12): 6288–6312. https://doi.org/10.1016/j.jcp.2008.03.007.

Appendix A—Analytical Solution to the Minimization Problem

The solution to the minimization problem (Eqs. 39 and 40) is equivalent to the following problem:

$$\text{Minimize } F(\mathbf{y}) = \frac{\left\| \frac{w_1}{l_1}(\mathbf{x}_A - \mathbf{y}) + \frac{w_2}{l_2}(\mathbf{x}_B - \mathbf{y}) \right\|}{\frac{w_1}{l_1} + \frac{w_2}{l_2}}, \quad \text{(A-1)}$$

$$\text{subject to } \|\mathbf{y} - \mathbf{x}_f\| \le R'. \quad \text{(A-2)}$$

Because the denominator of Eq. A-1 is positive, objective function $F(\mathbf{y})$ can be manipulated algebraically to the following form:

$$F(\mathbf{y}) = \frac{\left\| \frac{w_1}{l_1}(\mathbf{x}_A - \mathbf{y}) + \frac{w_2}{l_2}(\mathbf{x}_B - \mathbf{y}) \right\|}{\frac{w_1}{l_1} + \frac{w_2}{l_2}} = \left\| \frac{\frac{w_1}{l_1}(\mathbf{x}_A - \mathbf{y}) + \frac{w_2}{l_2}(\mathbf{x}_B - \mathbf{y})}{\frac{w_1}{l_1} + \frac{w_2}{l_2}} \right\| = \left\| \frac{\frac{w_1}{l_1}\mathbf{x}_A + \frac{w_2}{l_2}\mathbf{x}_B}{\frac{w_1}{l_1} + \frac{w_2}{l_2}} - \mathbf{y} \right\|. \quad \text{(A-3)}$$

We recognize that the first term of $F(\mathbf{y})$ is nothing but the original definition of harmonic-averaging point given by Eq. 34. Therefore, the objective function is simplified as

$$F(\mathbf{y}) = \|\mathbf{y}_\sigma - \mathbf{y}\|. \quad \text{(A-4)}$$

Considering a face σ as shown in Fig. 5, solution to the optimization problem (Eqs. A-1 and A-2) can be found directly as the intersection point between the line connecting $\mathbf{x}_f$ and $\mathbf{y}_\sigma$ and the circle centered at $\mathbf{x}_f$ with radius R'. For 2D problems, the solution can be found analogously.

Wenjuan Zhang is a PhD-degree candidate in petroleum engineering at Khalifa University of Science and Technology, Abu Dhabi, UAE. His main research interests are discretization methods for reservoir simulation. Zhang holds a bachelor's degree in petroleum engineering and a master's degree in oil and gas field development engineering, both from China University of Petroleum (East China). He also holds an MS degree in petroleum engineering from the Petroleum Institute in Abu Dhabi.

Mohammed Al Kobaisi is an associate professor in petroleum engineering at Khalifa University of Science and Technology, Abu Dhabi, UAE. Previously, he was the Energy Affairs Manager during his ministerial post at the UAE Ministry of Foreign Affairs in 2015 and 2016 and Deputy Permanent Representative of the UAE Mission to the International Renewable Energy Agency in 2016 and 2017. In 2011 and 2012, Al Kobaisi was a visiting faculty member at Stanford University. He has authored or coauthored numerous papers in refereed journals, has presented at technical meetings, and has coauthored one book. Al Kobaisi holds BSc, MSc, and PhD degrees from the Colorado School of Mines, all in petroleum engineering. He is actively involved in SPE and serves as a technical reviewer for *SPE Journal* and *SPE Reservoir Evaluation & Engineering*. Al Kobaisi is also a technical reviewer for the *Journal of Petroleum Exploration and Production Technology*, and a member of the Society for Industrial and Applied Mathematics and the European Association of Geoscientists and Engineers.